Density correction of NRLMSISE-00 in the middle atmosphere (20–100 km) based on TIMED/SABER density data

Xuan Cheng [1,2], Junfeng Yang [1], Cunying Xiao [1,*], Xiong Hu [1]

[1] National Space Science Center, Chinese Academy of Sciences, Beijing, 100190, China
[2] University of Chinese Academy of Sciences, Beijing, 100049, China

Correspondence to: Cunying Xiao (xiaocunying@bnu.edu.cn)

Abstract. This paper describes the density correction of the NRLMSISE-00 using more than 15 years (2002–2016) of TIMED/SABER satellite atmospheric density data from the middle atmosphere (20–100 km). A bias correction factor dataset is established based on the density differences between the TIMED/SABER data and NRLMSISE-00. Seven height nodes are set in the range 20–100 km. The different scale oscillations of the correction factor are separated at each height node, and the spherical harmonic function is used to fit the coefficients of the different timescale oscillations to obtain a spatiotemporal function at each height node. Cubic spline interpolation is used to obtain the correction factor at other heights. The spatiotemporal correction function proposed in this paper achieves a good correction effect on the atmospheric density of the NRLMSISE-00 model. The correction effect becomes more pronounced as the height increases. After correction, the relative error of the model decreased by 40–50% in July, especially at ±40 °N in the 80–100 km region. The atmospheric model corrected by the spatiotemporal function achieves higher accuracy for forecasting the atmospheric density during different geomagnetic activities. During geomagnetic storms, the relative errors in atmospheric density at 100 km, 70 km, and 32 km decrease from 41.21%, 22.09%, and 3.03% to −9.65%, 2.60%, and 1.44%, respectively, after correction. The relative errors in atmospheric density at 100 km, 70 km, and 32 km decrease from 68.95%, 21.02%, and 3.56% to 3.49%, 2.20%, and 1.77%, respectively, during geomagnetic quiet period. The correction effect during geomagnetic quiet period is better than that during geomagnetic storms at a height of 100 km. The subsequent effects of geomagnetic activity will be considered, and the atmospheric density during magnetic storms and quiet periods is corrected separately near 100 km. The ability of the model to characterize the mid-atmosphere (20–100 km) is significantly improved compared with the pre-correction performance. As a result, the corrected NRLMSISE-00 can provide more reliable atmospheric density data for scientific research and engineering fields such as data analysis, instrument design, and aerospace vehicles.

1 Introduction

The middle atmosphere (20–100 km) is affected by the lower troposphere. For example, the upload of tropospheric Rossby internal waves causes stratospheric planetary-scale disturbances in winter (Huang, et al., 2018, Matsuno, 1970) and the uploading of tropospheric gravity waves to the middle atmosphere (Alexander, 1996). The 20–100 km zone can also be affected

by the thermosphere and the upper atmosphere, such as in the reduction of ozone content caused by particle sedimentation (Rozanov, et al., 2012, Semeniuk, et al., 2011). The coupling of the upper atmosphere and the lower atmosphere with the middle atmosphere causes complex physical and chemical changes in the middle atmosphere. Neutral density is an important environmental parameter in the middle atmosphere. The atmospheric experience model is an important means of obtaining neutral density. Atmospheric experience models are indispensable in science and engineering, and are widely used in data analysis and engineering design (Kim, et al., 2012, Namgaladze, et al., 2006, Park, et al., 2008, Qian, et al., 2018, Yurasov, et al., 2008). The MSIS series, CIRA series, and Jacchia series are commonly used empirical models of the atmosphere. These empirical atmospheric models are capable of characterizing the climate change characteristics of atmospheric density. However, because of the irregular spatial and temporal distribution of the observation data, different detection errors from different devices, and simplifications used to establish the atmospheric model, there will be some differences between the atmospheric model and the actual atmosphere (Chen, et al., 2014, Lathuillère and Menvielle, 2010, Vielberg, et al., 2018, Xu, et al., 2006, Zhou, et al., 2009). Neutral density is the basic input parameter for aircraft design, and density errors between models and observations are one of the main sources of error in spacecraft orbit determination, orbit prediction, and reentry return point prediction. Reducing the differences between atmospheric models and the real atmosphere is a problem that is continually being addressed. Developments in detection technology and the continuous accumulation of data provide an important foundation for the verification, correction, and improvement of current models.

Various correction studies have considered atmospheric empirical models using observations of density data. For example, the MSIS series of models continues to enrich its database by constantly updating the data source and recalculating the model coefficients using the latest data. Satellite resistance data, accelerometer data, and 95–130 km incoherent scatter radar data were added to the latest version, NRLMSISE-00 (M. Picone, et al., 2002). In addition, using the difference between measured data and the model output to establish the spatiotemporal function of the model correction factor is an effective method for correcting empirical atmospheric models. To modify the JR-71 model, Bergstrom et al. (2002) proposed a linear correction term for the LEO orbital atmospheric density model based on observation data. This method improved the accuracy of the model. Chen et al. (2013) used GRACE and CHAMP satellite density data to correct NRLMSISE-00. The correction effect was verified by a three-day short-term forecast test. The results showed that the corrected model prediction error had been reduced by more than 50%, significantly improving the prediction accuracy of the model for atmospheric density. Zhou et al. (2009) obtained the relationship from the thermal mass density to the Joule heating power and the high-resolution loop current index by statistically analyzing thermal-layer atmospheric density data from the CHAMP satellite accelerometer during a magnetic storm. Modifying NRLMSISE-00 using an empirical relationship enables better predictions of the atmospheric density during a magnetic storm. Shi et al. (2015) calculated the ratio of the atmospheric density of the two line elements (TLE) inversion to that of NRLMSISE-00 based on 36 LEO satellite TLE data points from 2000–2002, and calibrated the error in the NRLMSISE-00 output. The results show that the relative root mean square error of NRLMSISE-00 had decreased by approximately 9% after calibration. Mehta et al. (2017) proposed a method for building a semi-physical model driven by thermal layer data using orthogonal decomposition. NRLMSISE-00 was calibrated using GRACE and CHAMP density data

to obtain a more accurate atmospheric density. Zhang et al. (2018) modified the Jacchia–Roberts empirical atmospheric model using a correction method based on empirical orthogonal function decomposition. This resulted in the 30-day average relative deviation of atmospheric density decreasing by 9.06%. The HASDM model is a modification of Jacchia based on 75 satellite orbit data. The correction method relies on precise orbit determinations, and is costly. Numerous studies on calibrating the density of atmospheric models have used neural network techniques. Perez and Bevilacqua (2015) used the densities from DTM-2013, NRLMSISE-00, and JB2008 as the neural network targets, with CHAMP and GRACE satellite data used for training, verification, and testing. The resulting density error was better than that before correction. The above studies considered altitudes in the thermosphere, namely the satellite orbital heights. For example, the orbital height of GRACE is about 500 km, and that of CHAMP is about 454 km.

Although there have been some studies on atmospheric model correction methods, they mainly focus on the thermalsphere, particularly the satellite orbital height. There have been no relevant reports on calibrating empirical atmospheric models at heights of 20–100 km. In this paper, NRLMSISE-00 is used as the modified target model. We construct a spatiotemporal correction function of the model density at 20–100 km for the first time. To evaluate the correction results, statistical methods are used to compare the difference between the atmospheric model and the observed data before and after correction over the period 2002–2016. Observation data from 2017 are used to evaluate the correction effect of the spatiotemporal correction function on the atmospheric density during geomagnetic storms and geomagnetic calm periods. The improved accuracy of the empirical atmospheric model provides more reliable data support for scientific research and engineering fields such as data analysis, numerical simulation, instrument design, and aircraft design.

2 Data source and methods

2.1 Database

Thermosphere Ionosphere Mesosphere Energetics and Dynamics (TIMED) is the first solar exploration mission in the NASA Solar Linkage Program. TIMED was launched on December 7, 2001, and has been accumulating data for over 17 years. The satellite orbit is a sun-synchronous orbit at a height of about 625 km and an orbital inclination of 74.1 °. The period of the satellite orbiting the Earth is about 1.6 h. Sounding of the Atmosphere Using Broadband Emission Radiometry (SABER) uses the edge detection method to detect infrared radiation from CO_2 in the atmosphere and invert parameters such as atmospheric temperature and density. These data are used to understand the energy exchange and kinetic processes of the intermediate layer, low thermal layer, and low ionosphere, mesosphere and lower thermosphere (MLT) region. They are also useful for determining basic pressure, temperature, and wind field characteristics due to energy input and output (Mertens, et al., 2009, Russell, et al., 1999). Satellite precession is slow, taking about 60 days to complete 24 h coverage of local time. Processed raw density data are meshed in the height direction by quality control steps such as preprocessing, information range checking, extreme value checking, and vertical consistency checking (Xiao, et al., 2016, Xiao, et al., 2017). The grid resolution is 1 km from 20–100 km. In the NRLMSISE-00 model, density is calculated under the same latitude, longitude, local time,

geomagnetic activity, and solar activity as the satellite trace. The model values are meshed in the height direction in the same way as the observation data.

2.2 Correction method

Define the relative error in density between NRLMSISE-00 and TIMED/SABER as:

$$\delta(\%) = \frac{\rho_M - \rho(h)}{\rho(h)} \quad (1)$$

Where $\rho_M(h)$ is the model density and $\rho(h)$ is the observed density.

Define the correction factor *R* as:

$$R = \frac{\rho(h)}{\rho_M(h)} \quad (2)$$

$$\delta(\%) = \frac{1}{R} - 1 \quad (3)$$

The correction factor *R* is directly related to the relative error of NRLMSISE-00. We use the gridded observation data and the model to calculate *R* using Eq. (2). Referring to the modeling method of NRLMSISE-00 below the thermosphere, we set seven height nodes in the range 20–100 km (at 100 km, 90 km, 72 km, 55 km, 45 km, 32 km, and 20 km). At heights of 100 km, 90 km, and 72 km, considering the errors caused by inaccuracies in the tidal wave and traveling planetary wave representations of atmospheric models, spatiotemporal correction functions are established. At the other four height nodes, the errors caused by inaccuracies in the planetary wave representation of the atmospheric model are considered, and spatiotemporal correction functions are established at the remaining height nodes. Cubic spline interpolation is used to calculate the correction factor at other heights. The correction factor for each height node is meshed with a horizontal resolution of $4^\circ \times 5^\circ$ and a time resolution of 1 h. The data are divided into latitude, longitude, and local time of the 120-day window centered on the day that meshing occurred. In theory, it takes 60 days for the satellite data to cover the global 24 h of local time. Satellite observation data cannot cover the 24 h of local time at high latitudes in this 60-day window because of the satellite adjustment attitude. Therefore, the meshing of *R* uses a 120-day sliding window with 1-day steps.

Equation (4) is used to separate 8-h, 12-h, 24-h, 2-day, 6-day, 10-day, 16-day, and 24-day oscillations of *R* in each horizontal grid at 100 km, 90 km, and 72 km (Pancheva and Mukhtarov, 2011, Xu, et al., 2006).

$$R = R_1 + \sum_{i=1}^{5}\left(R_{1i}\cos\left(\frac{2\pi}{T_i}tloc\right) + R_{2i}\sin\left(\frac{2\pi}{T_i}tloc\right)\right) + \sum_{j=1}^{3}\left(R_{1j}\cos\left(\frac{2\pi}{T_j}tloc\right) + R_{2j}\sin\left(\frac{2\pi}{T_j}tloc\right)\right) \quad (4)$$

Where R_1 is the correction factor average, $R_i = \sqrt{R_{1i}^2 + R_{2i}^2}$ and $\varphi_i = \frac{2\pi}{T_i}\tan^{-1}\left(\frac{R_{2i}}{R_{1i}}\right)$ $(i = 1{\sim}5)$ represent the amplitude and phase of components with periods of 2, 6, 10, 16, and 24 days, respectively; $R_j = \sqrt{R_{1j}^2 + R_{2j}^2}$ and $\varphi_j = \frac{2\pi j}{24}\tan^{-1}\left(\frac{R_{2j}}{R_{1j}}\right)$ $(j = 1{\sim}3)$ represent the amplitude and phase of components with periods of 24, 12, and 8 h, respectively. Further, the annual and semi-annual changes in the above timescale components of the correction factor are separated.

The oscillation components of the annual, semi-annual, quasi-biennial, and 11-year variations of the average term R_1 are separated. The spherical time harmonic function is fitted to the different timescale component datasets to obtain a modified function coefficient set.

For the other height nodes, the zonal mean of R is calculated, and the annual, semi-annual, quasi-biennial, and 11-year variations of the correction factor are fitted in each latitude. A fourth-order Fourier function is used to fit the zonal variation of different timescale components to obtain different timescale component coefficient sets of the correction function. The residual dataset is obtained by subtracting the long-term variation component from the horizontal grid data. The spherical harmonic function is fitted to the residual dataset of each height node to obtain a coefficient set of the smaller timescale components of the correction function.

2.3 Method of assessment

The model density and the observed density from 2002–2016 were meshed before and after correction (grid resolution $2.5^{\circ} \times 2.5^{\circ}$). The relative error of the model density before and after correction relative to the observed density was then calculated. The relative error of the multi-year average density value of the model before and after correction relative to the multi-year observed average was also calculated, and then the difference before and after correction was compared.

To test the effect of the correction function during different types of geomagnetic activity, the uncorrected observation data from 2017 were selected to evaluate the correction effect of the atmospheric model under different geomagnetic conditions. Observation data from a geomagnetic quiet period and a magnetic storm were selected, and the average relative error and standard deviation of the atmospheric model density before and after correction were calculated. The forecasting effect of the atmospheric model before and after correction was then compared.

3 Results

3.1 Difference between model and observations

There are many studies on the characteristics of atmospheric density variations based on observation data. The atmospheric density has characteristic variations in both the vertical and horizontal directions. In the vertical direction, the atmospheric density decreases exponentially with height, and seasonal variations are significant. At a fixed height, the density of the summer hemisphere is greater than that of the winter hemisphere. The density in the middle and low latitudes is higher than that in the high latitudes in the spring and autumn. In the stratosphere, planetary wave 1 and wave 2 structures exist at mid-high latitudes in the northern hemisphere in January, and the planetary wave 1 structure exists in the southern hemisphere. There is no obvious planetary wave structure in the two hemispheres in July. The horizontal structure of the density in the mesosphere in winter and summer is similar to that in the stratosphere. The main difference in the distribution is between that in spring and that in autumn. The density at the equator is lower than that at mid-latitudes at the height of the stratosphere, whereas it is higher at the height of the mesosphere. In the thermosphere, the density attains a maximum value over the Antarctic in January

and over the Arctic in July. In spring and autumn, the equator density is higher than that in the northern and southern hemispheres. Perturbations in density can be used to characterize the relative intensity of atmospheric fluctuations. These perturbations in atmospheric density also exhibit seasonal variations. The relative perturbation in atmospheric density increases with height in the vertical direction. The density perturbation in the northern hemisphere is higher than that in the southern hemisphere in January, and the perturbation in density near 60 °latitude in the southern hemisphere reaches its maximum value in July. During the transition periods of spring and autumn, the density perturbation at the equator is lower than that in the northern and southern hemispheres.

Figure 1 compares the NRLMSISE-00 output with observations. Figure 1(a) clearly shows the difference between the model and observations at 90 km. In the vicinity of 60°N and −30°N, the relative error of the model attains maximum values of 68% and 62%, respectively, in June–July. In the vicinity of −60 ℃N and 30 ℃N, the maximum relative error of the model is 63% and 60%, respectively in December. At 60 km, the relative error of atmospheric model at low and medium latitudes is mainly around 15%. From December to January, the maximum value of the relative error of atmospheric model in low latitudes can reach 23%. At 30 km, the relative error maximum value is 7% in the low latitude area from January to April. In the mid-latitudes of the southern hemisphere, there is a minimum value near August, with a relative error of -5%.

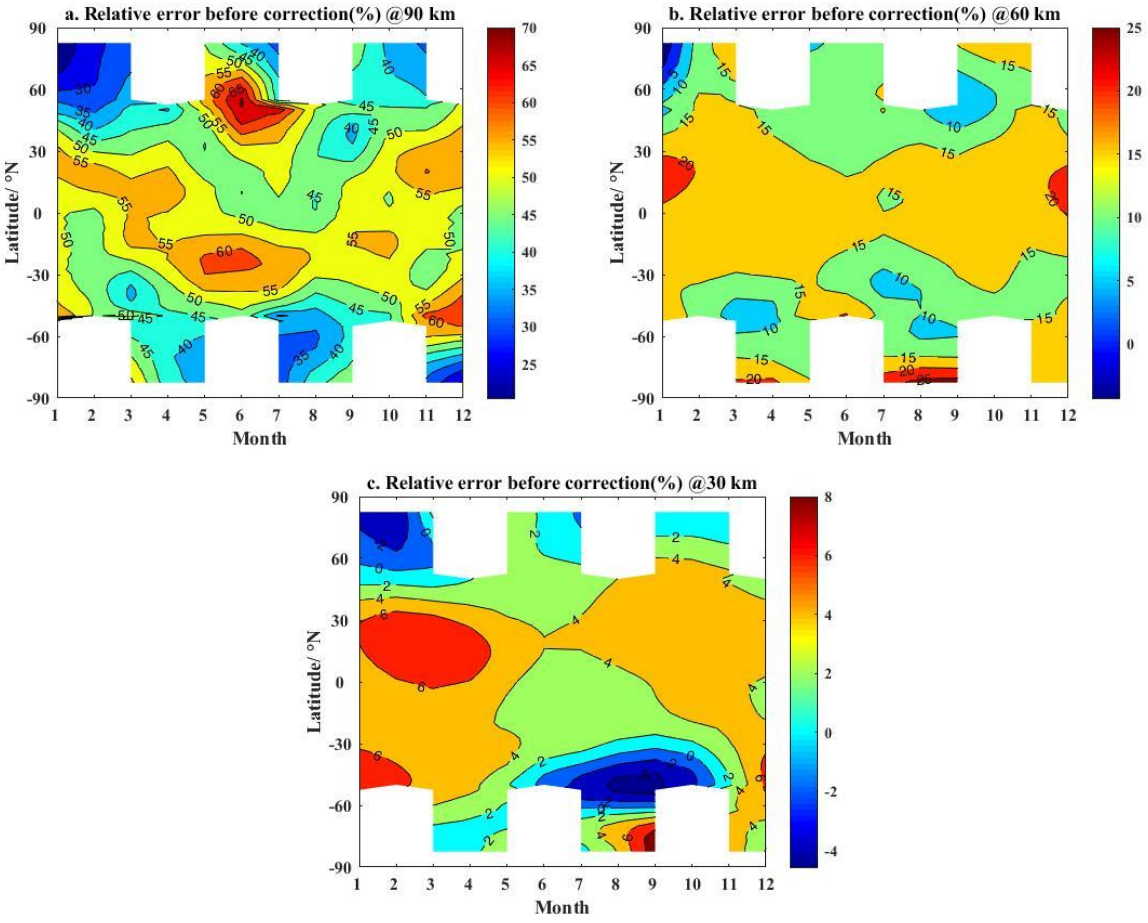

Figure 1: Latitude–month cross-section of relative error before correction. a. at 90 km; b. at 60 km; c. at 30 km.

As shown in Figure 2, the relative error in model density increases with height for the same latitude. The relative error at middle and low latitudes is higher than that at high latitudes from 80–100 km. Near the equator in January, the maximum relative error of the model reaches 79% at 100 km. From 45–80 km, the relative error of the model in the northern hemisphere is greater than that in the northern hemisphere. In July, the relative error is mainly around 50%, with the maximum reaching 68% at 80-100 km. From 45–80 km, the relative error of the model at middle and low latitudes in the northern hemisphere is greater than that at high latitudes in the northern hemisphere. In contrast, the relative error of the model at middle and low latitudes in the southern hemisphere is less than that at high latitudes in the southern hemisphere. Below about 45 km, the relative error of the model is generally less than 10%. Atmospheric planetary waves, atmospheric tidal waves and atmospheric gravity waves are important sources of atmospheric disturbances above 70 km (Pancheva and Mukhtarov, 2011, Xiao, Hu, Wang and Yang, 2016, Zhang, et al., 2006). The atmospheric density of the NRLMSISE-00 model is calculated from the atmospheric temperature. In the UMLT region, there is a large error between the model temperature and the TIMED/SABER observation (Xuan, et al., 2018). The contribution of traveling planetary waves to atmospheric disturbances and the inaccurate

estimation of atmospheric tides are the possible reasons for the large error of atmospheric temperature in the UMLT region. The atmospheric model transmits the error caused by the inaccurate representation of the atmospheric temperature disturbance to the atmospheric density, which makes the atmospheric density have larger errors in the UMLT region.

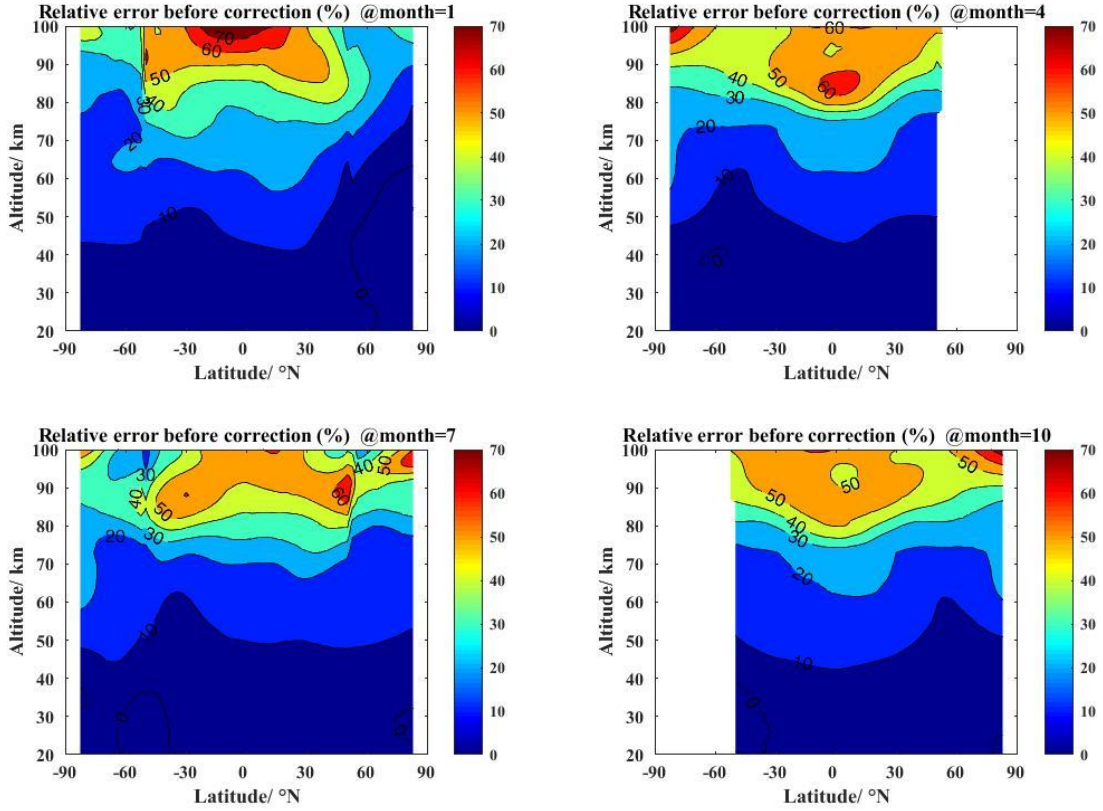

Figure 2: Latitude-height cross-section of relative error before correction in January, April, July, and October.

3.2 Statistical correction results

(1) Latitude–month

Figure 3 shows the latitude–month cross-section of the zonal mean relative error in the calibrated model at different heights. At 90 km, the relative error of the calibrated atmospheric model has a maximum value of 19% near 60 ℃N in June and July. Compared with the relative error of the model before correction, the the relative error of calibrated model reduces the maximum from 68% to 19% in the vicinity of 60 ℃N from June to July. The maximum error decreases from 62% to 7% near −30 ℃N. At 60 km, the relative error of calibrated model reduces the maximum from 23% to less than 4% near equator in December-January after correction. And in the vicinity of -80 ℃N, the the relative error of calibrated model reduces the maximum from

20% to 3% in April and 26% to 4% in August. At 30 km, the the relative error of calibrated model reduces the maximum from 7% to less than 2% in low latitudes in January to April.

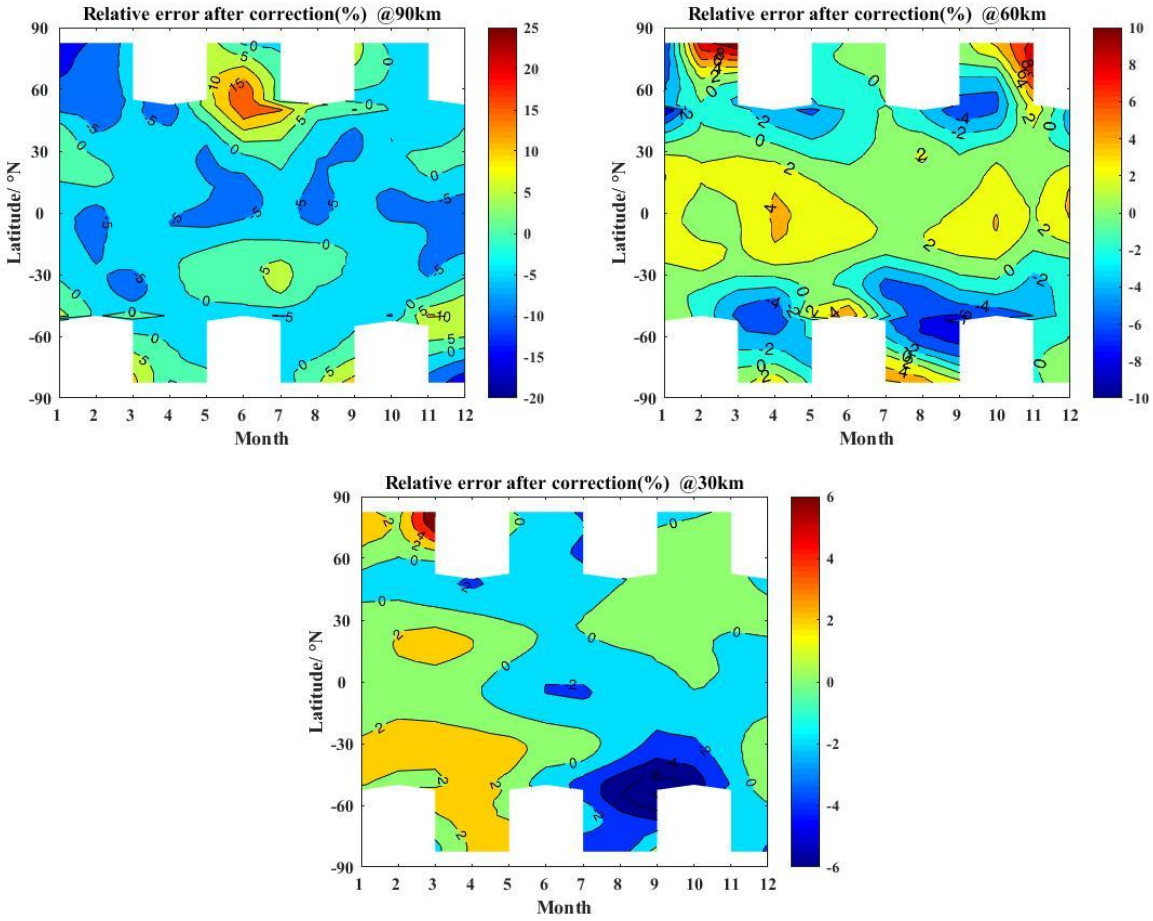

Figure 3: Latitude–month cross-section of relative error after correction at 90 km, 60 km and 30 km

(2) Latitude–altitudes

Figure 4 shows the latitude–height cross-section of relative deviations in the calibrated model in January, April, July, and October. As it can be seen from the figure that the correction effect of the atmospheric model is significant above 70 km. In January, the the relative error of calibrated model reduces the maximum from 79% to 17% at 100 km near equator. In April, the the relative error of calibrated model reduces the maximum from 64% to 16% around 80 km near equator. In July, the maxima occur at ±40 °N around 80–90 km, representing relative errors of 14% and 17%. In October, the the relative error of calibrated model has a maximum value of 12% around 80 km. From 20–70 km, the relative error of the calibrated model is small. Compared with Figure 2, it can be seen that the relative error between the calibrated data and the observations has been significantly reduced, especially in the middle and low latitudes at heights of 80–100 km.

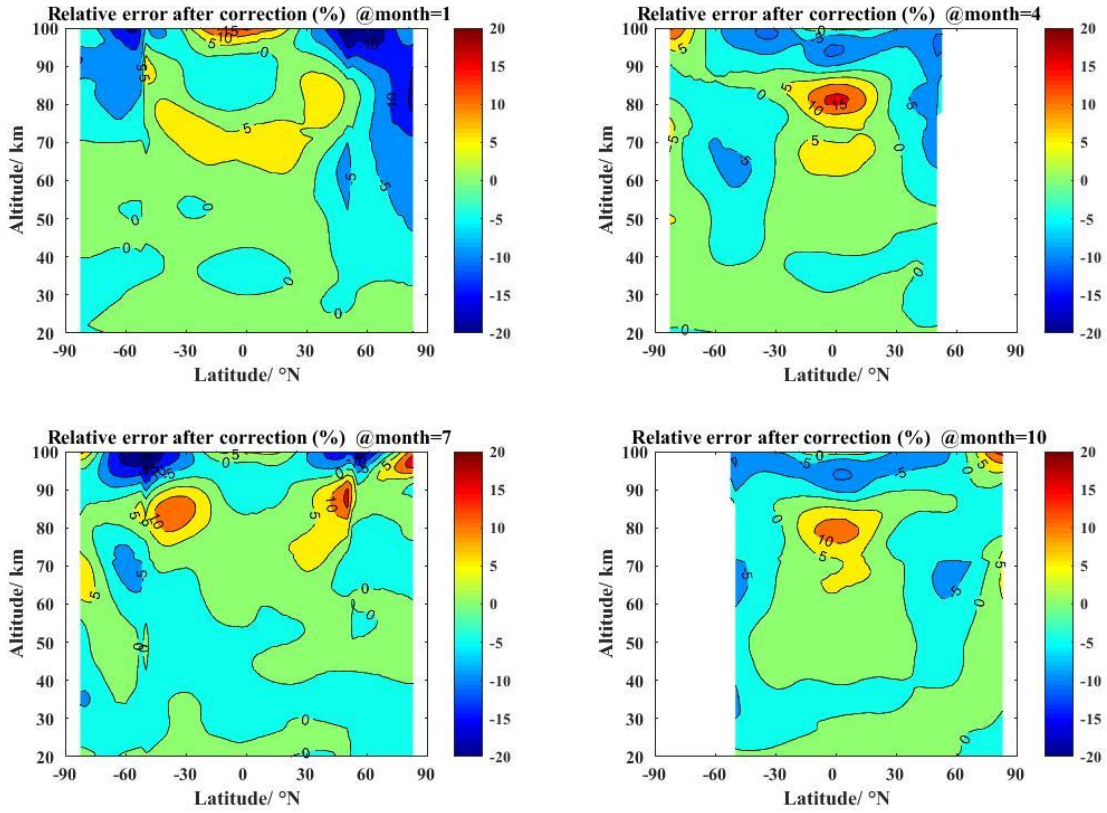

Figure 4: Latitude-height cross-section of relative error after correction in January, April, July, and October.

3.3 Correction results under different local time

In order to compare the correction results of different local times (LT), the relative error was calculated at different local times before and after the correction. Figure 5 shows the relative error of the atmospheric model before and after correction for different local time. At 90 km and 60 km, the relative error of the atmospheric model before correction is positive at different geographical locations, indicating that the model value is greater than the satellite observations. At 90 km, the relative error is between 30% and 100% befror correction and the relative error is between ±20% after correction. In the latitude of ±50 °N, the relative error has local maximum at about LT 6 and LT 19. The smallest relative error is seen in the LT range of about 10-14, but there is no more data in that LT range. In the latitude of ±30 °N, the relative error has a local maximum in the LT range of about 2-7, and there is a local minimum in the LT range of 14-18. At 60 km, the relative error is mainly between 5% and 25% befror correction and the relative error is mainly between ±5% after correction.

At 30 km, the relative error of the atmospheric model before correction has both positive and negative values at different local times and the relative error of the model has improved to some extent. At the same height, the relative error of the atmospheric

model varies with local time in the northern hemisphere is similar to that in the southern hemisphere. The relative error varies with local time in a similar sine or cosine function. It can be considered that the relative error has a relationship with the local time, as diurnal waves or semidiurnal waves.

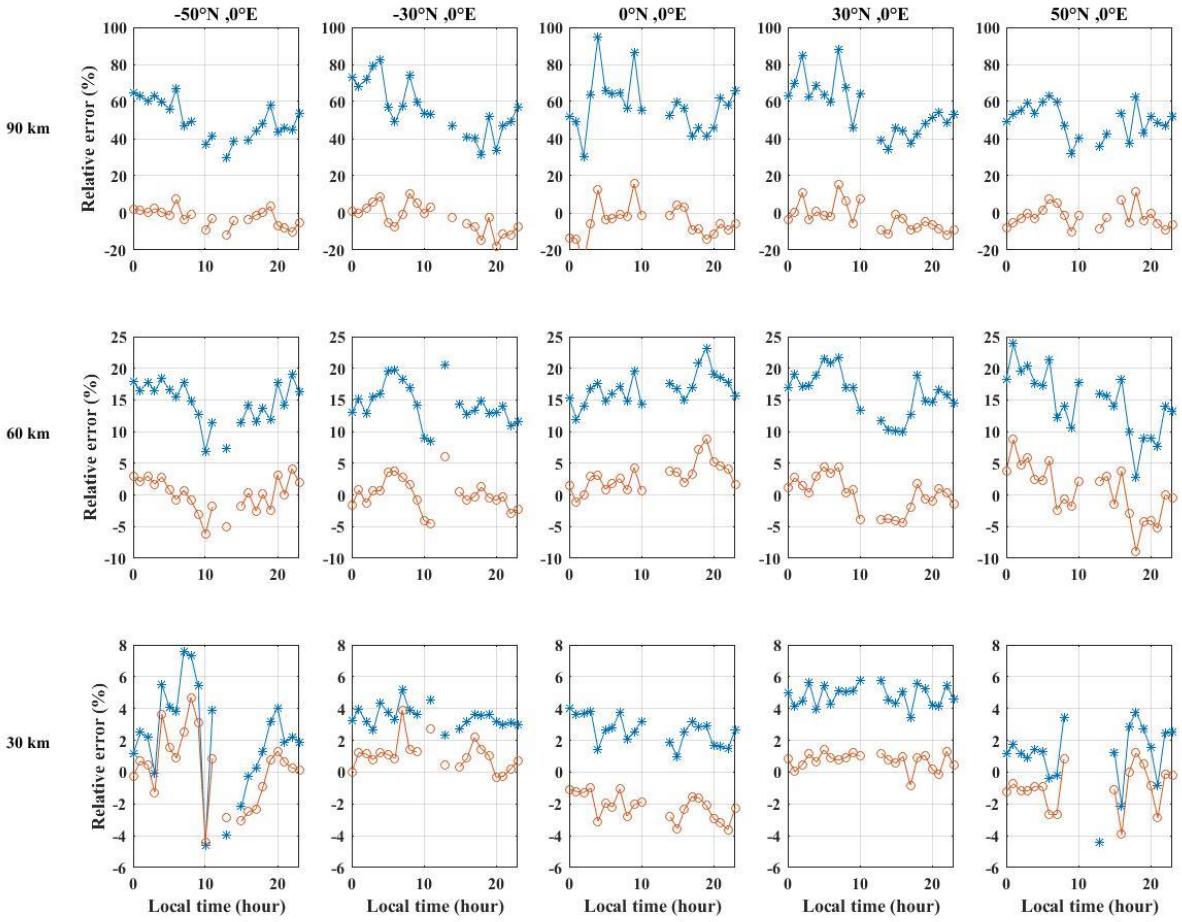

230

Figure 5: The relative error of the model varies with local time before (blue lines) and after (red lines) correction in 2008.

3.4 Correction results under different geomagnetic conditions

Density data from days with an Ap index greater than 80 and less than 27 were selected to calculate the correction effect during a geomagnetic storm and a geomagnetic quiet period, respectively. A large magnetic storm with an Ap index of 106 occurred
235 on September 8, 2017 (day 251), and this was used as the object for evaluating the model during a geomagnetic storm. Most of the days in 2017 were in the geomagnetic quiet period (Ap < 27). The geomagnetic Ap index measured just 5 on May 9,

2017 (day 129), and remained below 10 a few days either side of this day. Thus, the data from May 9, 2017 were selected to evaluate the model during a geomagnetic calm period.

The correction effects were analyzed at three altitude nodes (both node heights and non-node heights were contained), namely 100 km (representing the low thermosphere), 70 km (mesosphere), and 32 km (stratosphere). The density observations from SABER were extracted at these node heights on days 129 and 251. At the same time, the density and corrected density of NRLMSISE-00 were calculated under the same conditions. We then compared the forecast results given by the model before and after correction.

Figure 6 shows the atmospheric density during the geomagnetic storm at 100 km, 70 km and 32 km. There is a large deviation between the atmospheric density calculated by NRLMSISE-00 and that observed by SABER. The corrected model density is closer to the density observed by SABER. The correction effects at 70 km and 32 km are considerable. Table. 1 presents the statistical results for the relative error in the NRLMSISE-00 density before and after correction on day 251 and the average relative error and standard deviation of the corrected model density. During the geomagnetic storm, the average relative error of NRLMSISE-00 before correction is 41.42% and the standard deviation is 32.18%. After correction, the average relative error is −9.65% and the standard deviation is 22.56%. The absolute correction of the model is 31.56%. At 70 km, the average relative error before correction is 22.09% and the standard deviation is 7.74%. After correction, the average relative error is 2.60% and the standard deviation is 5.76%. This represents an absolute correction of 19.49%. At 32 km, the average relative error before correction is 3.03% and the standard deviation is 4.96%. This decreases to an average relative error of 1.44% and standard deviation of 4.29% after correction, with an absolute correction of 1.59%. Thus, the model is more accurate in characterizing the atmospheric density at these three node heights after error correction.

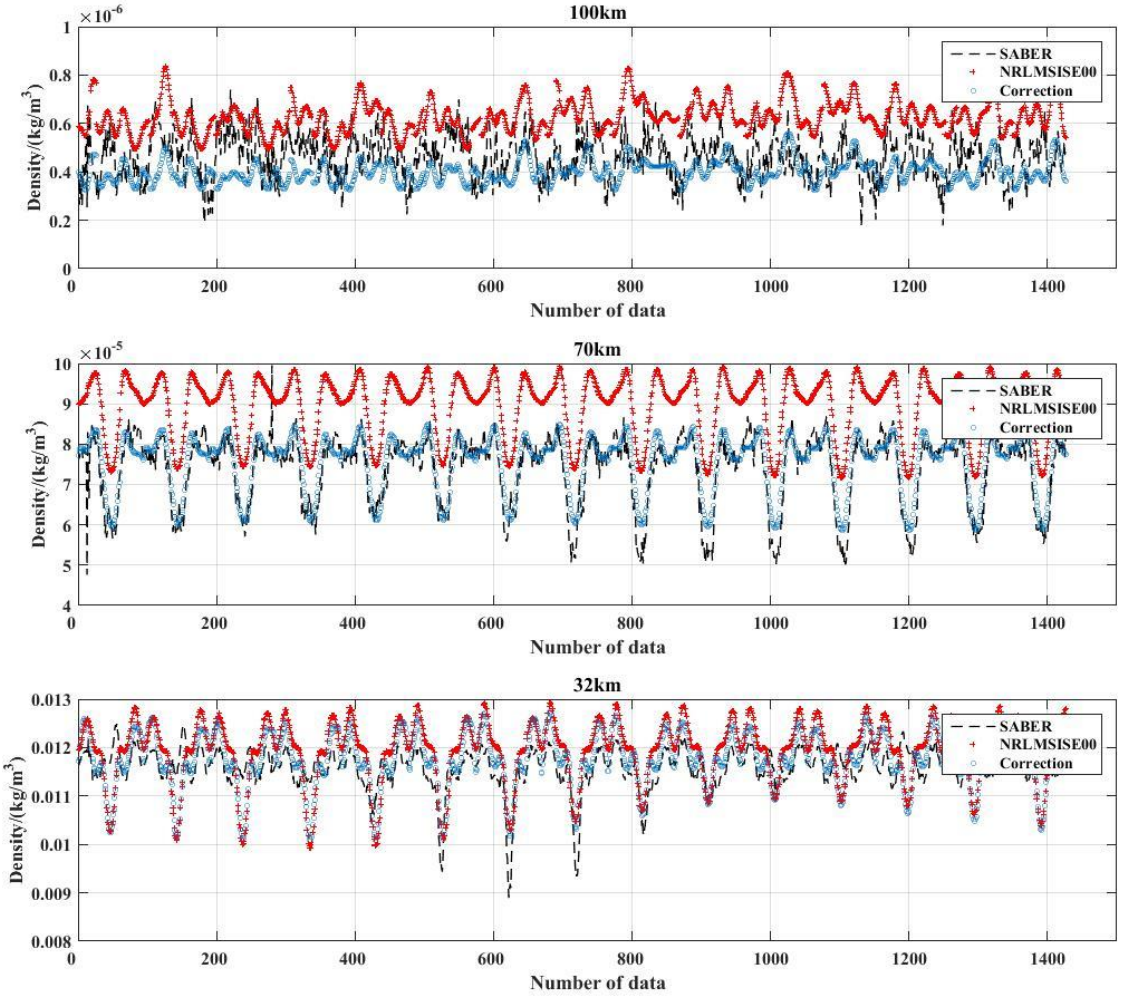

Figure 6: Density variations at different heights during a geomagnetic storm (day 251 of 2017). a. 100 km; b. 70 km; c. 32 km.

Table. 1 Atmospheric density error on satellite orbits at different nodes on day 251 of 2017 (%)

	100km		70km		32km	
	Mean	**Std**	**Mean**	**Std**	**Mean**	**Std**
NRLMSISE00	41.21	32.18	22.09	7.74	3.03	4.96
Correction	-9.65	22.56	2.60	5.76	1.44	4.29

Figure 7 shows that the density of the three nodes during geomagnetic quiet condition is closer to the SABER observations after correction. The statistical results for the relative error in Table. 2 indicate that the average relative error before correction is 68.95% with a standard deviation of 33.29% at 100 km. After correction, these values drop to 3.49% and 20.65%, respectively. The absolute correction of the model is 65.46%. Thus, correction significantly improves the accuracy of the density given by NRLMSISE-00 at 100 km in geomagnetic quiet periods. Before correction, the average relative error at 70 km is 21.02% and the standard deviation is 8.04%. The average relative error decreases to 2.20% with a standard deviation of 6.41% after correction. The absolute correction of the model is 18.82%. Thus, error correction of the NRLMSISE-00 model makes a considerable improvement in the accuracy of the atmospheric density at 70 km. At a height of 32 km, the average relative error before correction is 3.56% and the standard deviation is 1.57%. After correction, the average relative error is 1.77% and the standard deviation of the relative error is 1.91%, with an absolute correction of 1.79%. Again, the model accuracy has been improved by the error correction process.

The effect of the correction function varies under the different geomagnetic conditions at around 100 km. After correction, the relative error in the model density decreased from 68.95% to 3.49% during a period of geomagnetic quiet condition. During a magnetic storm, the relative error in model density decreased from 41.21% to −9.65%. The correction effect during geomagnetic quiet condition is better than that during a geomagnetic storm. In this study, the influence of geomagnetic activity is not considered in the process of establishing the correction function. This factor will be considered in future to improve the correction ability of the spatiotemporal correction function during magnetic storms and to enhance the model's ability to represent the actual atmosphere.

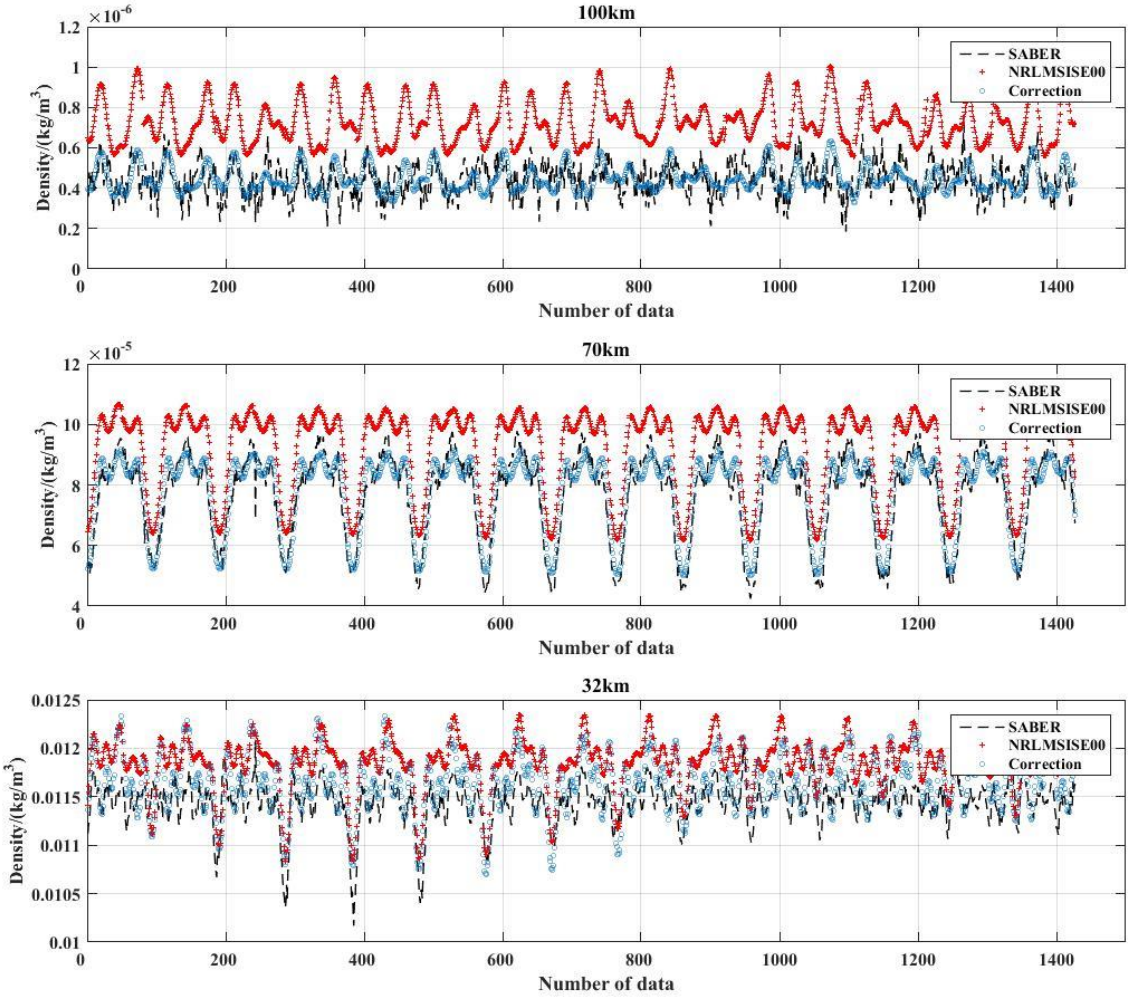

280

Figure 7: Same as Figure 6, but for day 129 of 2017.

Table. 2 Atmospheric density error on satellite orbits at different nodes on day 129 of 2017 (%)

	100km		70km		32km	
	Mean	**Std**	**Mean**	**Std**	**Mean**	**Std**
NRLMSISE00	68.95	33.29	21.02	8.04	3.56	1.57
Correction	3.49	20.65	2.20	6.41	1.77	1.91

4 Discussion

4.1 Discussion of the correction method

Considering the error caused by the inaccurate characterization of atmospheric model density as a result of seasonal variations, intra-annual variations, inter-annual variations, and changes in the 11-year cycle of solar activity, we incorporated the above factors into the correction function. In addition, considering the distribution of atmospheric fluctuations in the atmosphere with height, we divided the range 20–100 km into two height intervals. The first, 70–100 km, contains three height nodes, at 72 km, 90 km, and 100 km, whereas the second, 20–70 km, consists of four height nodes, at 20 km, 32 km, 45 km, and 55 km. To simplify the correction function, inaccuracies in the atmospheric tidal characterization were considered in the 70–100 km height interval. As the NRLMSISE-00 model does not consider traveling planetary waves, we integrated several traveling planetary wave periodic components into the correction function. At a height of 20–70 km, the atmospheric tide is relatively weak. Below 40 km, the contribution of atmospheric tidal components is small, and the contribution of planetary waves is significant, especially in the winter hemisphere. Therefore, the four height nodes in this interval only consider the atmospheric model to be inaccurate in the representation of planetary waves. To see the correction effect more intuitively, we define the absolute deviation of the relative error between the uncalibrated model and the calibrated model as $\Delta\delta = |\delta_{model}| - |\delta_{correct}|$, where $\Delta\delta$ is the absolute deviation of the relative error, δ_{model} is the relative error of the model before correction, and $\delta_{correct}$ is the relative error of the model after correction. $\Delta\delta > 0$ indicates that the model density after correction is closer to that observed by SABER, and the corrective effect is considerable. $\Delta\delta < 0$ indicates that the model density deviates more from the satellite observation of the atmospheric density after correction, i.e., the correction makes the estimate worse. According to Figure 8, the variation in the zonal mean of the model improves in this latitude–altitude cross-section in January, April, July, and October. (Winter and summer are represented by January and July, and spring and autumn are represented by April and October.) The figure shows that the overall effect of the correction function is significant at 20–100 km, and only the local area model improvement is negative. For example, in the high latitudes of the northern hemisphere in January and the southern hemisphere in April, and the mid-high latitudes of the southern hemisphere in October, the relative error of the corrected model was slightly greater than in the original model. For all areas where the improvement is negative in these months, the results are presented in Table. 3. In the region where $\Delta\delta < 0$ in January, the average value of the improvement was −0.43% and the standard deviation was 0.41%. In the region where the improvement is negative, the relative error of the modified model is less than 1% compared with that of the model before correction. In areas where the improvement is negative in other months, the average relative error of the model density before and after correction is again less than 1%. Therefore, the spatiotemporal correction function established in this study has a significant effect on the overall correction of the NRLMSISE-00 model.

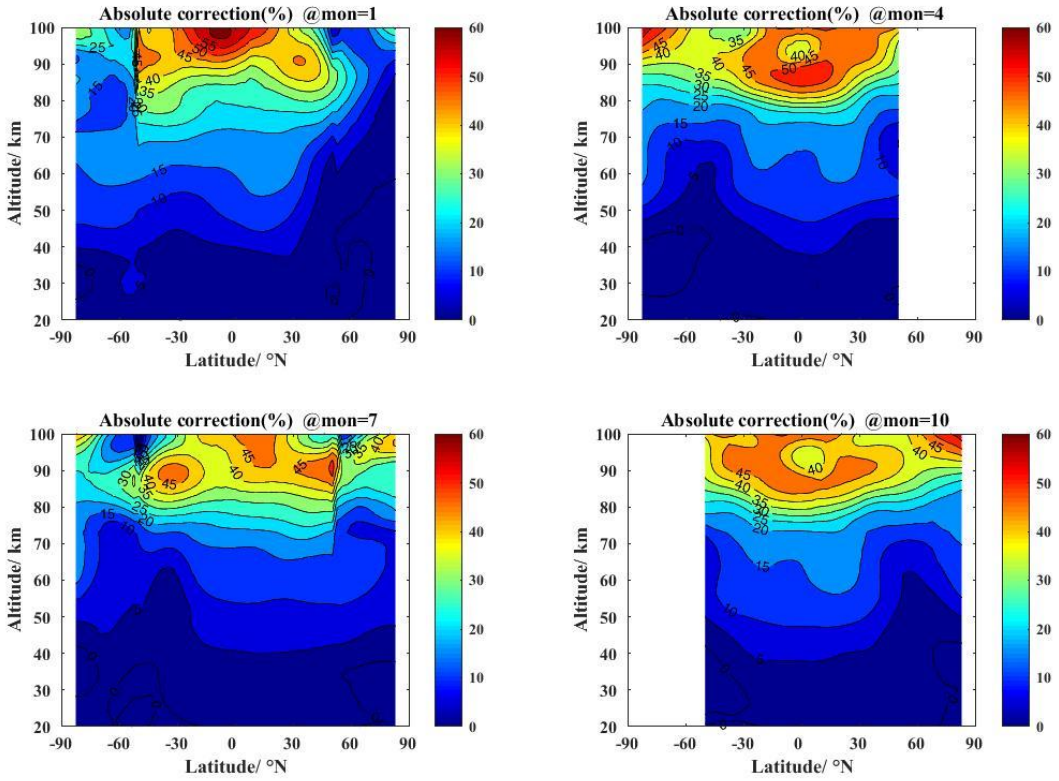

315

Figure 8: Latitude-height cross-section of $\Delta\delta$ in January, April, July, and October.

Table. 3 The average and standard deviations in the area of $\Delta\delta < 0$ (%)

January		April		July		October	
Mean	**Std**	**Mean**	**Std**	**Mean**	**Std**	**Mean**	**Std**
-0.43	0.41	-0.47	0.32	-0.81	0.90	-0.44	0.34

320

4.2 Influence of geomagnetic activity

During geomagnetic storms and substorms, a large number of high-energy particles are injected into the middle and upper atmosphere. There have been many studies on the influence of high-energy particle sedimentation on the middle atmosphere.
325 The atmosphere is excited and ionized by these high-energy particles, and the chemical composition of the atmosphere changes dramatically in terms of O_3, NO_x, and HO_x concentrations (Sinnhuber, et al., 2012, Zawedde, et al., 2016). Changes in these chemical components may cause heating and cooling of the atmosphere, which influences other processes in the middle atmosphere (Kishore Kumar, et al., 2018, Ogunjobi, et al., 2014, Pancheva, et al., 2007). However, there has been little research

on the temperature response of the mesosphere to the sedimentation of high-energy particles. Only a few studies have reported an increase in temperature at middle and high latitudes during energetic particle precipitation in the mesopause (Savigny, et al., 2007, Yuan, et al., 2015). There is a strong coupling between the ionosphere and the neutral atmosphere during geomagnetic storms. Both the ionosphere and the lower atmosphere exhibit quasi-two-day waves (QTDWs) in the geomagnetic quiet period because of upward coupling of QTDWs. During a minor sudden stratospheric warming (SSW), the amplitude of the QTDWs in the upper stratosphere is weakened and intensified after the geomagnetic storms. However, the QTDWs in the ionosphere are enhanced after geomagnetic storms. The possible reason is that the same frequence of interplanetary magnetic field and QTDWs with the modulation of different phase of storm induced circulation and the climatological circulations in the lower mesosphere might have led to enhancement and inhibition of the amplitude of the QTDWs over different hemisphere (Mengistu Tsidu and Abraha, 2014). Other studies have shown that the atmospheric density in the mesosphere over polar regions is negatively correlated with geomagnetic activity (Yi, et al., 2018, Yi, et al., 2017). The mechanism by which the atmospheric density in the mesosphere over polar zones responds to geomagnetic activity is considered to be different from that in the thermosphere (Lei, et al., 2008, Xu, et al., 2015). The results of these studies indicate that the response mechanism of mid-atmospheric density to geomagnetic activity requires further clarification and exploration to promote the establishment of new models and improve existing models.

4.3 Influence of solar activity

Solar activity is another important factor in correction factor modeling. From the modeling of temperature, NRLMSISE-00 calculates the density of each component using the physical relationship between the temperature, static equilibrium, and ideal gas state equation. The sum of the density in each of the components is the total density. The response of the NRLMSISE-00 atmospheric density to solar activity depends, to some extent, on the temperature response to solar activity. The sensitivity to solar activity varies with altitude, with studies showing that the effects of solar activity decrease with height. The absorption of solar radiation by ozone in the stratosphere plays an important part in the energy cycle and kinetics of the heating and cooling of the stratosphere. The changes are influenced by kinetics, chemistry, and other parameters (Staehelin, et al., 2001), while the 11-year solar cycle has little effect on the total ozone content (L. Hood, 1997). There are conflicting results regarding the response of MLT to solar activity. Luebken (2001) used sounding data to study the structural characteristics of the mesosphere over the polar regions in the past 35 years. The results indicate that the temperature structure of the mesosphere in this zone has not changed significantly. Detailed analysis showed that the solar cycle has little effect on temperature. However, Remsberg and Deaver (2005) used HALOE to examine temperature changes in the upper and middle stratosphere from 1991–2004 temperature data. In the upper and middle part of the tropical stratosphere, the temperature responded significantly to the solar activity week. In the upper part of the tropical stratosphere and the subtropical mesosphere, the trend suggested a linear decline, but this phenomenon has not been found in the tropical mesosphere. Therefore, the mechanism of the influence of solar activity on the middle atmosphere requires further study so that atmospheric models can better characterize the influence of solar activity on the middle atmosphere.

5 Conclusions

In this study, we used density data from TIMED/SABER for the period 2002–2016 to correct the density of the empirical atmospheric model NRLMSISE-00 at a height of 20–100 km for the first time. By analyzing the difference between the model output and the observations, a method for establishing a spatiotemporal correction function for NRLMSISE-00 was proposed. According to the spatiotemporal distribution characteristics of the correction factor dataset, different timescale oscillations in the correction factors appear at every node. The spherical harmonic function was used to fit the coefficients of the separated components to obtain the spatiotemporal correction function for NRLMSISE-00 over the range 20–100 km. The corrected model density was calculated using this function and the results were evaluated. To this end, the main conclusions from this study are as follows:

(1) The model and observations exhibit the same variation in the horizontal and vertical directions, but there is a certain deviation. The relative error of the model at middle and high latitudes is greater in the summer hemisphere than in the winter hemisphere. In addition, the relative error of the model increases with height in the vertical direction, especially in the region of 80–100 km.

(2) The accuracy of the calibrated model is better than that of NRLMSISE-00. The accuracy of the model is significantly improved at altitudes of 80–100 km.

(3) The correction function produces a significant improvement in the prediction of atmospheric model density under different geomagnetic conditions. After correction, the relative errors in model density at 100 km, 70 km, and 32 km decreased from 41.21%, 22.09%, and 3.03% to −9.65%, 2.60%, and 1.44%, respectively, during an geomagnetic storm. During a geomagnetic quiet period, the relative errors in model density at 100 km, 70 km, and 32 km decreased from 68.95%, 21.02%, and 3.56% to 3.49%, 2.20%, and 1.77%, respectively. In the low thermosphere, the correction effect of the function in the geomagnetic calm period is significantly better than that in the magnetic storm period. Subsequent work will consider the effects of geomagnetic activity and optimize the ability of the spatiotemporal correction function to correct the atmospheric density during magnetic storms.

The density mechanism in response to solar activity and geomagnetic activity requires further investigation in the range 20–100 km. This theoretical study provides a technical basis for the establishment of new models and the improvement of existing models, and enhances the ability of NRLMSISE-00 to represent the real atmosphere. By correcting the density over the range 20–100 km for NRLMSISE-00, higher-quality initial and background fields can be provided for numerical simulations and predictions in scientific research. Additionally, reliable atmospheric density data can be derived for aircraft design, simulation, and flight tests in aerospace and other engineering fields.

Author contribution

Xuan Cheng and Cunying Xiao have made contributions to the conception and design of this work. Xuan Cheng and Junfeng Yang have made contributions to the acquisition, analysis and interpretation of data and creation 355 of spatiotemporal

correction function. Xuan Cheng have drafted the manuscript and Cunying Xiao and Xiong Hu have revised it critically for important intellectual content.

Author contribution

The authors declare that they have no conflict of interest.

Acknowledgements

This study was supported by the National Key Research and Development Program of China (2016YFB0501503), the Strategic Priority Research Program of Chinese Academy of Sciences Grant No. XDA17010301, the National Natural Science Foundation of China (Grant No. 11872128). We thank the TIMED/SABER working group (http://saber.gats-inc.com/data_services.php) to provide the observation data and the Space Environment Forecast Center of the National Space Science Center of the Chinese Academy of Sciences to provide the F10.7 and Ap index.

References

Alexander, J., 1996. A Simulated Spectrum of Convectively Generated Gravity Waves: Propagation from the Tropopause to the Mesopause and Effects on the Middle Atmosphere. Journal of Geophysical Research 101 (D1), 1571-1588.

Bergstrom, S.E., Proulx, R.J., Cefola, P., 2002. Atmospheric density correction using observational data, AIAA/AAS Astrodynamics Specialist Conference and Exhibit

Chen, H.R., Liu, H.X., Hanada, T., 2014. Storm-time atmospheric density modeling using neural networks and its application in orbit propagation. Advances in Space Research 53 (3), 558-567.

Chen, X., Hu, X., Xiao, C., Wang, X., 2013. Correction method of the low earth orbital neutral density prediction based on the satellites data and NRLMSISE-00 model. Chinese J . Geophys. (in Chinese) 56 (10), 3246-3254.

Huang, R., Chen, W., Wei, K., Wang, L., Huangfu, J., 2018. Atmospheric dynamics in the stratosphere and its interaction with tropospheric processes: Progress and problems. Chinese Journal of Atmospheric Sciences 42 (3), 463-487.

Kim, J.S., Urbina, J.V., Kane, T.J., Spencer, D.B., 2012. Improvement of TIE-GCM thermospheric density predictions via incorporation of helium data from NRLMSISE-00. Journal of Atmospheric and Solar-Terrestrial Physics 77, 19-25.

Kishore Kumar, G., Nesse Tyssøy, H., Williams, B.P., 2018. A preliminary comparison of Na lidar and meteor radar zonal winds during geomagnetic quiet and disturbed conditions. Journal of Atmospheric and Solar-Terrestrial Physics 168, 70-79.

L. Hood, L., 1997. The solar cycle variation of total ozone: Dynamical forcing in the lower stratosphere. Journal of Geophysical Research 102 (D1), 1355-1370.

Lathuillère, C., Menvielle, M., 2010. Comparison of the observed and modeled low- to mid-latitude thermosphere response to magnetic activity: Effects of solar cycle and disturbance time delay. Advances in Space Research 45 (9), 1093-1100.

Lei, J., Thayer, J., M. Forbes, J., K. Sutton, E., Nerem, R., Temmer, M., Veronig, A., 2008. Global thermospheric density variations caused by high-speed solar wind streams during the declining phase of solar cycle 23. Journal of Geophysical Research 113 (A11), A11303.

Luebken, F.-J., 2001. No long term change of the thermal structure in the mesosphere at high latitudes during summer. Advances in Space Research 28 (7), 947-953.

M. Picone, J., Hedin, A.E., P. Drob, D., Aikin, A., 2002. NRLMSISE-00 empirical model of the atmosphere: Statistical comparison and scientific issues. Journal of Geophysical Research 107 (A12), 1468.

Matsuno, T., 1970. Vertical Propagation of Stationary Planetary Waves in the Winter Northern Hemisphere. Journal of Atmospheric Sciences 27 (6), 871-883.

Mehta, P.M., Linares, R., 2017. A methodology for reduced order modeling and calibration of the upper atmosphere. Space Weather 15 (10), 1270-1287.

Mengistu Tsidu, G., Abraha, G., 2014. Moderate geomagnetic storms of January 22–25, 2012 and their influences on the wave components in ionosphere and upper stratosphere-mesosphere regions. Advances in Space Research 54 (9), 1793-1812.

Mertens, C., Russell Iii, J., Mlynczak, M., She, C.-Y., J. Schmidlin, F., Goldberg, R., López-Puertas, M., P. Wintersteiner, P., Picard, R., Winick, J., Xu, X., 2009. Kinetic temperature and carbon dioxide from broadband infrared limb emission measurements taken from the TIMED/SABER instrument. Advances in Space Research 43 (1), 15-27.

Namgaladze, A.A., Zubova, Y.V., Namgaladze, A.N., Martynenko, O.V., Doronina, E.N., Goncharenko, L.P., Van Eyken, A., Howells, V., Thayer, J.P., Taran, V.I., Shpynev, B., Zhou, Q., 2006. Modelling of the ionosphere/thermosphere behaviour during the April 2002 magnetic storms: A comparison of the UAM results with the ISR and NRLMSISE-00 data. Advances in Space Research 37 (2), 380-391.

Ogunjobi, O., Sivakumar, V., Sivla, W.T., 2014. A superposed epoch study of the effects of solar wind stream interface events on the upper mesospheric and lower thermospheric temperature. Advances in Space Research 54 (9), 1732-1742.

Pancheva, D., Mukhtarov, P., 2011. Atmospheric Tides and Planetary Waves: Recent Progress Based on SABER/TIMED Temperature Measurements (2002–2007). 19-56.

Pancheva, D., Singer, W., Mukhtarov, P., 2007. Regional response of the mesosphere–lower thermosphere dynamics over Scandinavia to solar proton events and geomagnetic storms in late October 2003. Journal of Atmospheric and Solar-Terrestrial Physics 69 (9), 1075-1094.

Park, J., Moon, Y.J., Kim, K.H., Cho, K.S., Kim, H.D., Kwak, Y.S., Kim, Y.H., Park, Y.D., Yi, Y., 2008. Comparison between the KOMPSAT-1 drag derived density and the MSISE model density during strong solar and/or geomagnetic activities. Earth, Planets and Space 60 (6), 601-606.

Perez, D., Bevilacqua, R., 2015. Neural Network based calibration of atmospheric density models. Acta Astronautica 110, 58-76.

Qian, L.Y., Burns, A.G., Solomon, S.S., Smith, A.K., McInerney, J.M., Hunt, L.A., Marsh, D.R., Liu, H.L., Mlynczak, M.G., Vitt, F.M., 2018. Temporal Variability of Atomic Hydrogen From the Mesopause to the Upper Thermosphere. Journal Of Geophysical Research-Space Physics 123 (1), 1006-1017.

Remsberg, E.E., Deaver, L.E., 2005. Interannual, solar cycle, and trend terms in middle atmospheric temperature time series from HALOE. Journal Of Geophysical Research-Atmospheres 110 (D6), D06106.

Rozanov, E., Calisto, M., Egorova, T., Peter, T., Schmutz, W., 2012. Influence of the Precipitating Energetic Particles on Atmospheric Chemistry and Climate. Surveys in Geophysics 33 (3), 483-501.

Russell, J.M., Mlynczak, M.G., Gordley, L.L., Tansock, J., Esplin, R., 1999. An overview of the SABER experiment and preliminary calibration results. Optical Spectroscopic Techniques And Instrumentation for Atmospheric And Space Research Iii 3756, 277-288.

Savigny, C., Sinnhuber, M., Bovensmann, H., Burrows, J., Kallenrode, M.B., Mj, S., 2007. On the disappearance of noctilucent clouds during the January 2005 solar proton events. Geophysical Research Letters 34 (2), L02805.

Semeniuk, K., Fomichev, V.I., McConnell, J.C., Fu, C., Melo, S.M.L., Usoskin, I.G., 2011. Middle atmosphere response to the solar cycle in irradiance and ionizing particle precipitation. Atmos. Chem. Phys. 11 (10), 5045-5077.

Shi, C., Li, W., Min, L., Zhao, Q., Sang, J., 2015. Calibrating the scale of the NRLMSISE00 model during solar maximum using the two line elements dataset. Advances in Space Research 56 (1), 1-9.

Sinnhuber, M., Nieder, H., Wieters, N., 2012. Energetic Particle Precipitation and the Chemistry of the Mesosphere/Lower Thermosphere. Surveys in Geophysics 33 (6), 1281-1334.

Staehelin, J., R. P. Harris, N., Appenzeller, C., Eberhard, J., 2001. Ozone trends: A review. Reviews of Geophysics 39 (2), 231.

Vielberg, K., Forootan, E., Luck, C., Locher, A., Kusche, J., Borger, K., 2018. Comparison of accelerometer data calibration methods used in thermospheric neutral density estimation. Annales Geophysicae 36 (3), 761-779.

Xiao, C.Y., Hu, X., Wang, B., Yang, J.F., 2016. Quantitative studies on the variations of near space atmospheric fluctuation. Chinese J . Geophys. (in Chinese) 59 (4), 1211-1221.

Xiao, C.Y., Hu, X., Yang, J.F., Yan, Z.A., Liu, T., Cheng, X., 2017. Characteristics of atmospheric density at 38 °N in near

space and its modeling technique. Journal of Beijing University of Aeronautics and Astronautics 43 (9), 1757-1765.

Xu, J., K. Smith, A., Yuan, W., Liu, H., Wu, Q., Mlynczak, M., 2006. The Global Structure and Long Term Variations of the Temperature Observed by TIMED/SABER. Journal of Geophysical Research 112 (D24), D24106.

Xu, J., Qiao, J., Wei, Y., Ruiping, M., 2006. Comparison between the TIMED observed global temperature distribution and the NRLMSISE-00 empirical atmospheric model. Chin. J . Space Sci. 26 (3), 177-182.

Xu, J., Wang, W., Zhang, S.-R., Liu, X., Yuan, W., 2015. Multiday thermospheric density oscillations associated with variations in solar radiation and geomagnetic activity: Thermospheric density oscillations. Journal of Geophysical Research: Space Physics 120 (5), 3829-3846.

Xuan, C., Cunying, X., Xiong, H., Junfeng, Y., 2018. Evaluation of atmospheric empirical model based on TIMED/SABER satellite temperature data. Sci Sin-Phys Mech Astron 48 (10), 79-93.

Yi, W., Reid, I., Xue, X., J. Murphy, D., M. Hall, C., Tsutsumi, M., Ning, B., Li, G., P. Younger, J., Chen, T., Dou, X., 2018. High- and Middle-Latitude Neutral Mesospheric Density Response to Geomagnetic Storms. Geophysical Research Letters 45 (1), 436-444.

Yi, W., Reid, I., Xue, X., P Younger, J., J Murphy, D., Chen, T., Dou, X., 2017. Response of neutral mesospheric density to geomagnetic forcing. Geophysical Research Letters 44 (16), 8647-8655.

Yuan, T., Zhang, Y., Cai, X., She, C.Y., Paxton, L., 2015. Impacts of CME Induced Geomagnetic Storms on the Mid-latitude Mesosphere and Lower Thermosphere Observed by a Sodium Lidar and TIMED/GUVI. Geophysical Research Letters 42 (18), 7295-7302.

Yurasov, V.S., Nazarenko, A.I., Alfriend, K.T., Cefola, P.J., 2008. Reentry time prediction using atmospheric density corrections. Journal Of Guidance Control And Dynamics 31 (2), 282-289.

Zawedde, A., Nesse Tyssøy, H., Hibbins, R., Espy, P., Ødegaard, L.-K., Sandanger, M.I., Stadsnes, J., 2016. The Impact of Energetic Electron Precipitation on Mesospheric Hydroxyl during a Year of Solar Minimum: EEP IMPACT ON MESOSPHERIC OH DURING SOLAR MINIMUM. Journal of Geophysical Research: Space Physics 121 (6), 5914-5929.

Zhang, H., Gu, D., Duan, X., Wei, C., 2018. Atmospheric density model calibration using emperical orthogonal function. Acta Aeronautica et Astronautica Sinica 39 (S1), 722263.

Zhang, X., Forbes, J.M., Hagan, M.E., Russell, J.M., Palo, S.E., Mertens, C.J., Mlynczak, M.G., 2006. Monthly tidal temperatures 20–120 km from TIMED/SABER. Journal of Geophysical Research 111.

Zhou, Y.L., Ma, S.Y., Lühr, H., Xiong, C., Reigber, C., 2009. An empirical relation to correct storm-time thermospheric mass density modeled by NRLMSISE-00 with CHAMP satellite air drag data. Advances in Space Research 43 (5), 819-828.